Applied Catalysis B: Environment and Energy 345 (2024) 123701

Contents lists available at ScienceDirect

Applied Catalysis B: Environment and Energy

journal homepage: www.elsevier.com/locate/apcatb

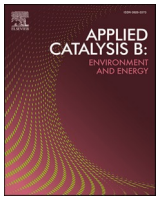

2D surfaces twisted to enhance electron freedom toward efficient advanced oxidation processes

Ximeng Xu [a], Shujing Zhang [a], Yuhao Wang [a], Nana Wang [a], Qinli Jiang [a], Xiaohong Liu [b], Qingqing Guan [a,*], Wei Zhang [c,*]

[a] Faculty of Civil Engineering and Mechanics, Kunming University of Science and Technology, Kunming 650500, China
[b] National University of Singapore (Chongqing) Research Institute, Chongqing 401123, China
[c] Chongqing Institute of Green and Intelligent Technology, Chinese Academy of Sciences, Chongqing 400714, China

ARTICLE INFO

Keywords:
2D Materials
Structural regulation
Lattice distortion
Twisted surface
Peroxymonosulfate

ABSTRACT

Two-dimensional (2D)-interface engineering for designing effective electron-rich catalyst center is pivotal in manipulating the catalytic behaviors and activity, but still challenging. Here, we've successfully twisted the surfaces of the 2D layered FeOCl, fulfilling the targeted fine-tuning of its Fe sites. The obtained new catalyst can boost peroxymonosulfate activation for reactive species with much lower energy barriers and efficiently oxidized target organic with almost 41 orders of magnitude faster reaction kinetics than pristine FeOCl. The increased degree of freedom of electron around Fe site has been identified as the key driver. The distorted geometry structure around Fe has led to an increased polarization of charge distribution, associating with less symmetric electron valence cloud and higher electron mobility. Thus, the twisted surfaces enable a much enhanced interfacial charge transfer between Fe site and the electron-deficient peroxymonosulfate. This work highlights the concept of twisted surface construction toward efficient advanced oxidation catalyst design.

1. Introduction

The presence of organic microcontaminants (OMCs) in water has been threatening aquatic ecosystems and human health, even at very low concentration [1,2]. Peroxymonosulfate (PMS) based advanced oxidation processes (AOPs) [3–5], i.e. Fenton-like reaction, has been deemed as a highly practical technology to produce reactive oxygen species (ROS) for OMCs oxidation. Transition metals [6–10] are most commonly used persulfate activators for ROS production. Compared with the homogeneous metal ions, their counterpart heterogeneous metal oxides possess wider working pH range, better adaptability as well as easier recovery, attracting a continuous growing interesting.

Normally, to produce ROS in heterogeneous AOPs, the initial step is to achieve electron transfer via the adsorption of peroxide onto the metal sites. Therefore, the orientated manipulation of these sites toward higher electron transfer rates [11–13] is critical for the development of more efficient AOPs, which still remains highly challenging. The chemical environment of active sites on the solid catalyst surface affect their intrinsic catalytic performance significantly [11]. It's therefore potential to design the surface geometrical structure of metals to regulate the reactions in AOPs precisely [14–16]. For instance, by regulating the chemical environment of Fe in FeOOH using series of ligands [17], the electron donation capacity has been enhanced with the increase of charge density around Fe and the length of Fe−O bond, leading to a much more efficient Fenton-like process.

Recent researches indicated that metal oxides with two-dimensional (2D) layered structure have highly controllable properties. As heterogeneous catalysts, it is generally considered that the unsaturated coordinative atoms at their surface edges are active centers of each layer [18], while the saturated atoms in the base planes seldom serve as catalytic active sites, somehow wasting their advantages of high specific surface area [19]. Thus, 2D-interface engineering including defect introduction, surface modification, and phase transition [20–22] have been developed as a novel frontier to make the most of properties of 2D materials, aiming at highly active catalysts exploiting. Thereinto, the regulated 2D layered materials with twisted surfaces has been claimed to demonstrate huge potential to create active surface regions, which may be attributed to the coordination field distortions of active center [19,23].

The construction of twisted surface onto 2D materials might offer an

* Corresponding authors.
E-mail addresses: 155455488@qq.com (Q. Guan), zhangwei@cigit.ac.cn (W. Zhang).

https://doi.org/10.1016/j.apcatb.2024.123701
Received 13 November 2023; Received in revised form 2 January 2024; Accepted 4 January 2024
Available online 6 January 2024
0926-3373/© 2024 Elsevier B.V. All rights reserved.

alternative strategy to design more efficient electron-donating catalysts. However, the 2D metal oxides with twisted surfaces have been very poorly explored as AOPs catalysts for a long time. Besides, quite limited regulation strategies based on twisted surface construction have been proposed so far for the precise manipulation of active site, leading to the huge knowledge vacuum in the 2D-interface engineering for AOPs. Additionally, elucidating how the twisted surfaces is related to the catalytic behavior can be of great significance, since the information is crucial for the targeted design of active sites toward effective and selective catalytic reactions [23].

Herein, we first constructed twisted surfaces onto the base planes of FeOCl, a typical 2D layered ferrite [24,25], via the intercalation of hydroxylamine (HA) into the layer structure. The work aims to provide a mechanism insight into the relationship between the surface twisting and the electron donation behavior, as well as the catalytic performance of Fe sites toward PMS activation. To our delight, compared to pristine FeOCl, the as-prepared HA-FeOCl showed evidently boosted activation rate toward PMS to generate ROS for OMCs degradation. After intercalation, the surface lattices of FeOCl experienced severe twisting, with unsaturated Fe coordination field forming and wide fluctuation in atomic bond distances and angles. Mössbauer spectra, X-ray absorption fine structure (XAFS) spectra, combining with Density Functional Theory (DFT) calculation, have been conducted to reveal the relationship between the twisted surface and the enhanced catalytic activity. This study provides a new strategy for heterogeneous AOP catalyst design at atomic level, and highlights the concept of 2D-interface engineering in manipulating catalytic oxidation reactions toward efficient environmental control.

2. Materials and methods

2.1. Chemicals and materials

Unless otherwise specified, all chemicals used in this study were of analytical grade. Ferric chloride hexahydrate ($FeCl_3$•6 H_2O, reagent grade, >98.0%), Hydroxylamine hydrochloride were obtained from Wind ship in Tianjin chemical reagent Co. Ltd. Hydroxylamine (HA, 50 wt% in H_2O), potassium peroxymonosulfate (PMS), bisphenol A (BPA), Rhodamine B (RhB), bisphenol S (BPS), sulfamethoxazole (SMX), carbamazepine (CBZ), Ibuprofen (IBU), Diclofenac, 2,4-Dichlorophenol (2,4-Dcp), L-Histidine (≥99.5%), β-Carotene (≥96%(HPLC)), Furfuryl alcohol (FFA), p-Benzoquinone (p-BQ) were purchased from Aladdin Industrial Corporation. Ethanol (EtOH), methanol (MeOH), tert-butanol (TBA) provided by Kelong Chemical Reagents Factory. Methyl phenyl sulfoxide (PMSO), methyl phenyl sulfone ($PMSO_2$) were purchased from Shanghai Macklin Reagent Co. Ltd., China. All solutions were prepared with ultrapure water generated from a Ulupure system.

2.2. Catalytic performance evaluation

In a typical experiment, 20 mg catalyst was added into 100 mL aqueous solution (containing organics) in a 250 mL beaker with stirring (550 rpm and 25 ± 2 °C) for 30 min to reach adsorption equilibrium. Afterwards, PMS at specific concentrations was added to beaker to initiate the reaction. At different time interval, 1.0 mL solution was removed and filtered using a 0.22 μm PTFE filter, followed by immediate quenching with excessive ROS quenchers, in order to determine the residue contaminant concentration. The quenching experiments were conducted by adding different scavengers, including tertiary butanol (TBA) and ethanol (EtOH) for $^{\bullet}OH$ and $SO_4^{\bullet-}$, p-benzoquinone (p-BQ) for $O_2^{\bullet-}$, Furfuryl alcohol (FFA), L-Histidine, and β-Carotene for $^1O_2$. Systematic evaluation of the catalytic reactivity of the samples involved the variations of different experimental parameters, including thed osage of catalyst, dosage of oxidant, pH values. The experimental equipment and conditions were identical to the general procedure.

Details of other methods, including synthesis of FeOCl and HA-FeOCl, characterization and analysis, electrochemical measurements, and density functional theory (DFT) calculation were given in the supporting information.

3. Results and discussion

3.1. Characterization of Catalysts

The schematic diagram in Fig. 1a elucidates the facile synthesis procedure of HA-FeOCl. The pristine FeOCl was directly immersed into the methanol solution containing HA for specific time to accomplish the intercalation. The as-prepared HA-FeOCl consists of nano-scale sheets with thickness of ~100–300 nm, which are randomly stacked in a coral-like architecture (Fig. 1b). Clearly, the HA-FeOCl has preserved the typical layered morphology feature of FeOCl (Fig.S3). The FESEM-mapping images (Fig. 1c) shows that N, which comes from HA, was roughly uniformly dispersed in the same position with Fe, O, and Cl, verifying the successful intercalation of HA into the layer structure of FeOCl. Fig. 1d shows the Fe 2p X-ray photoelectron spectroscopy (XPS) of FeOCl and HA-FeOCl. For both of them, the two major peaks corresponding to Fe $2p_{3/2}$ and Fe $2p_{1/2}$ were located at ~710.4 and ~724.1 eV, respectively. The Fe $2p_{3/2}$ can be well fitted into two peaks at binding energies of 710.7 eV and 713.4 eV, which can be ascribed to Oct Fe(II) and Oct Fe(III). It demonstrates the co-existence of Fe(II) and Fe (III), and noticeably, the relative content of Fe(II) calculated by the area of deconvoluted peaks increased from 28.17% to 57.32%, verifying the reduction of Fe(III) in the FeOCl matrix during intercalation.

Subsequently, ^{57}Fe Mössbauer spectroscopy was employed to precisely probe the change in Fe valence state and electronic configuration from pristine FeOCl and HA-FeOCl. As shown in Fig. 1e, the Mössbauer spectrum for both catalysts can be deconvoluted into two doublets by peak fitting (Table S1), attributing to Fe(II) and Fe(III), respectively. Based on the spectral area calculation, the ratio of Fe(II)/Fe(III) could be obtained. In comparison, after the intercalation, the ratio of Fe(III) dropped from 76.6% to 37.9%, while that of Fe(II) increased by 38.7%, further confirming the reduction of Fe. The isomer shift (IS) for Fe(II) was observed to decrease from 0.40 mm/s to 0.31 mm/s, and that for Fe (III) decreased from 0.21 mm/s to 0.15 mm/s (Table S1), it reflects that the bond length of Fe—Fe in FeOCl was shortened with an enhanced interaction [26] and the electron cloud density of Fe s orbit has increased [27,28]. Besides, the quadrupole splitting (QS) for both Fe(II) and Fe(III) has increased, from 0.87/0.91 mm/s to 0.98/0.95 mm/s, indicating that the shape of valence electron cloud around Fe nucleus has gradually transformed to ellipsoidal from spherical [29] (Fig. 1f).

XRD analysis (Fig. 2a) was conducted to investigate the structural evolution during the intercalation process. The pristine FeOCl showed reflections at 2θ values consistent with the standard pattern of FeOCl (JCPDS NO.24–1005), while all HA-FeOCl samples (with intercalation times of 4 h, 8 h, 24 h, and 48 h) showed peaks (~10°) shifting toward smaller angles, demonstrating the interlayer expansion, but the specific surface area of HA-FeOCl only increased to 3.5880 m^2/g (from 2.9836 m^2/g of FeOCl, Fig. S19), it implies that the expansion degree was relatively low. Clearly, the [010] orientation, which is perpendicular to the z axis, dominated the preferential facet growth, demonstrating the predominance of [010] orientation in HA-FeOCl. The disapperence of other typical peaks may be attributed to the changes in lattice parameters after the intercalation. The pristine FeOCl has a layered structure similar to γ-FeOOH and belongs to the orthorhombic space group of *Pmmn* with unit cell dimensions of a= 3.776 Å, b= 7.842, c= 3.304 Å [26]. Accordingly, the XRD pattern of HA-FeOCl was modeled based on the similar unit cell, with constants of a= 3.792 Å, b= 6.638 Å, c= 3.486 Å. As reported in previous studies [18,20,30], the variation in lattice constants could be ascribed to the lattice distortion. This can be further confirmed by the clearly observed lattice distortion in the High-resolution transmission electron microscopy (HRTEM) (Fig. 2b), the crystal planes with spacing values of 0.398 nm can be

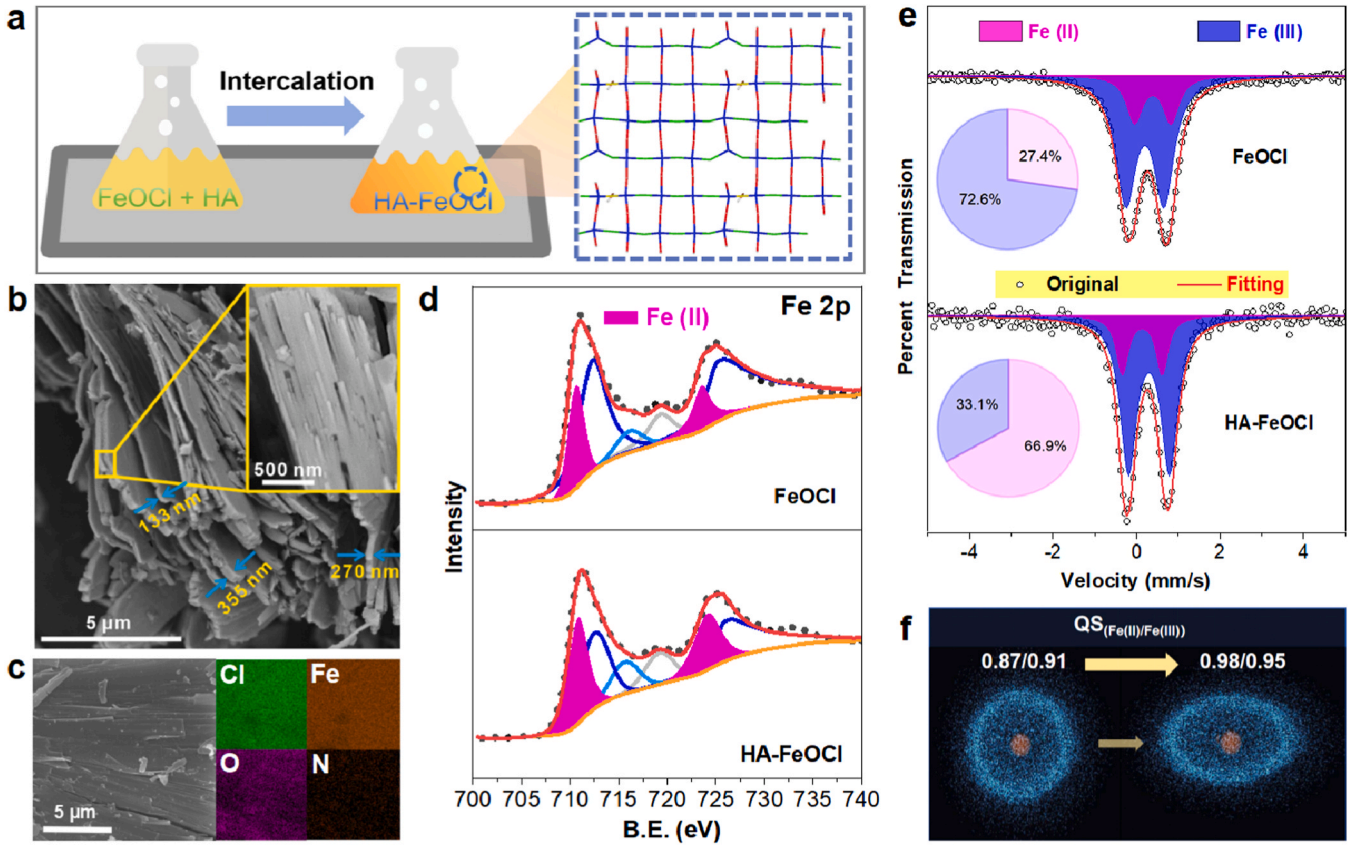

Fig. 1. Topography and valence characterizations. (a) Schematic diagram displaying the preparation of the HA-FeOCl. (b) FESEM picture and (c) FESEM-mapping pictures of HA-FeOCl. (d) Fe 2p survey spectra for FeOCl and HA-FeOCl. (e) Mössbauer spectra for FeOCl and HA-FeOCl. (f) Shape variation of electron cloud.

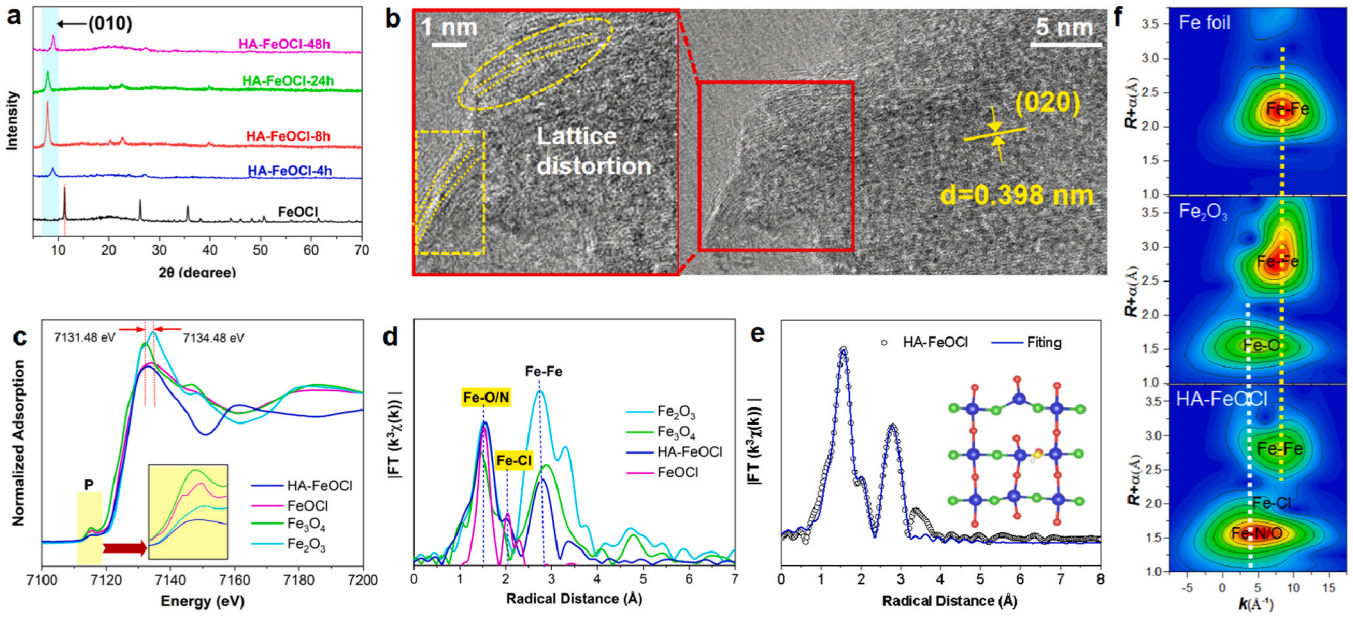

Fig. 2. Crystal structural and coordination environment characterizations. (a) XRD patterns for FeOCl and HA-FeOCl with different intercalation time. (b) High-resolution TEM image of the HA-FeOCl surface. (c) XANES spectra. (d) Fourier transform extended X-ray absorption fine structure (FT-EXAFS) spectra of different samples. (e) corresponding EXAFS R-space fitting curve of HA-FeOCl. (f) Wavelet transformation for the k^2-weighted EXAFS signal of HA-FeOCl and reference samples.

assigned to the (020) planes of FeOCl.

Lattice distortion is normally associated with the changes in coordination environment of Fe during the reductive intercalation process. To verify this, and further elucidate the coordinative structure of HA-FeOCl, the X-ray absorption near-edge structure (XANES) spectroscopy was conducted. Fig. 2c shows the Fe K-edge XANES spectra for FeOCl

and HA-FeOCl, together with Fe_2O_3 and Fe_3O_4 as reference compounds. The highest K–edge absorption energy of Fe in FeOCl appeared at 7133.4 eV, which was located between Fe_3O_4 (7132.1 eV) and Fe_2O_3 (7134.48 eV), proving the co–existences of Fe(II) and Fe(III) in FeOCl and the average valance between Fe_3O_4 and Fe_2O_3. While for HA-FeOCl, it appeared at 7132.7 eV, locating between FeOCl and Fe_3O_4, demonstrating the lower average valance of Fe in HA-FeOCl than that of FeOCl. Notably, in all spectra, a small pre-edge peak denoted as P at ~7115 eV can be observed, which has generally assigned to the 1 s to 3d dipolar forbidden transition. Based on previous XANES studies [30–33] on ferric model compounds, this peak loses its intensity from a direct quadrupole coupling to the electromagnetic radiation or a mixing of the 3d and 4p orbitals caused by the breakdown of inversion symmetry due to structural distortion. Consequently, as the local symmetry around the Fe is lowered from octahedral symmetry to tetrahedral symmetry, the intensity (I) of this peak tends to decrease. In the case of HA-FeOCl, the intensity of this peak is weaker than those of Fe_3O_4 and FeOCl (inset of Fig. 2c), indicating that the local coordinative structure around Fe became less symmetric after the intercalation. This is in accordance with the conclusions of Mössbauer spectroscopy. The Fourier transform (FT) EXAFS R–space fitting curve of HA-FeOCl (Fig. 2d) presents three major peaks at ~1.53 Å, ~2.02 Å, and ~2.73 Å. In reference to Fe_2O_3, Fe_3O_4, and FeOCl, these peaks can be assigned to the first shell of Fe–O/N and the second shell of Fe–Cl and Fe–Fe, respectively [30]. Comparing to FeOCl, the intensity for Fe–O/N peak increased while that for Fe–Cl decreased, indicating that parts of Cl atoms might be substituted during the intercalation.

As shown in the curve fitting of EXAFS results of HA-FeOCl (Fig. 2e, Table S2), each Fe atom is coordinated by ~3.0 O atoms and ~1.1 Cl atoms in average (~5.0 O atoms and ~0.8 Cl atoms in average for pristine FeOCl). The decreased coordination number of Fe atom corresponds to the variations of lattice parameters, which may directly lead to some substantial electronic changes onto the FeOCl surface.

Thereafter, combing with the information about composition and coordination environment of Fe sites, the geometric structure of HA-FeOCl was calculated in detail based on the first-principle density functional theory (DFT) computation and shown in Fig. 3a. Clearly, N atoms of HA have substituted parts of interlaminar Cl atoms, bonding with Fe directly (Eq. 1). The lone pair electrons of amines could transfer to the conduction band of FeOCl [34], which therefore explaining the reduction of Fe after the HA interlacation.

$$Fe{-}Cl + NH_2OH \rightarrow Fe{-}N{-}OH + 2\,H^+ + Cl^- \quad (1)$$

As a consequence, the Fe cluster was strongly distorted, as can be seen from Fig. 3b, comparing to the pritine FeOCl, the Fe atoms that boned with N as well as its adjacent Fe atoms all experienced great changes in Fe−O bond lengths and angles. For 2D layered materials, after the introduction of guest molecular into the interlamination, to stabilize the guest molecular, the layer tent to slide toward certain direction, leading to the lattice distortion as well as the twisting of the 2D surface. The appearance of the systematic extinction spots along the [010] direction in the Selected Area Electron Diffraction (SAED) pattern of HA-FeOCl (Fig. S4) suggested that the Fe-O-Cl layers slided (a+c)/2 in the ac-plane to stabilize the HA molecular, as illustrated in Fig. 3c.

3.2. Catalytic performance and involved ROS

Degradation of BPA in different catalytic systems were shown in Fig. 4a. As can be seen, only 3–4% of BPA were removed in the systems with individual PMS, HA-FeOCl, and FeOCl. In FeOCl/PMS system, 12% of BPA can be removed after 60 min, demonstrating the very limited catalytic ability of FeOCl toward PMS activation. While when HA (with same concentration of intercalated HA) was introduced separately, the BPA removal was accordingly enhanced to 37% (60 min). This could be attributed to the acceleration effect of HA to the Fe(II)/Fe(III) redox cycle [35]. Comparatively, HA-FeOCl/PMS system showed much higher oxidation activity with complete BPA removal within 20 min. Besides, the degradation rate (k_{obs}) of HA-FeOCl/PMS was determined to be 11.7 and 41.0 times higher than those of HA/FeOCl/PMS and FeOCl/PMS systems (Fig. 4b). Apparently, comparing with dosing HA directly into the heterogeneous reaction solution, loading it into the layer structure of FeOCl beforehand as part of the catalyst can be much more beneficial for PMS activation. It implies that the enhanced BPA oxidation capacity by HA-FeOCl/PMS dose not come from the acceleration effect of HA in the liquid phase. It is the variation of chemical environment around Fe that contributes to the much improved PMS activation capacity, which will be further elucidated and summarized in the following part.

HA-FeOCl could effectively oxidize a broad-spectrum of organics via PMS activation, but also exhibited a certain extent of selectivity (Fig. S12). Complete removal of Rhodamine B (RhB), Sulfamethoxazole (SMX), BPA, and Diclofenac can be achieved in 60 min, meanwhile, only 15% of bisphenol S (BPS), 36% of 2,4-Dichlorophenol (2,4-Dcp), 26% of Carbamazepine (CBZ), and 55% of Ibuprofen (IBU) were degraded. The reactivity of HA-FeOCl was discovered to be strongly correlated to the ionization potential (IP) values of organics (Fig. 4c, Table S3). Clearly, the system prefers to degrade organics with lower IP values (≤

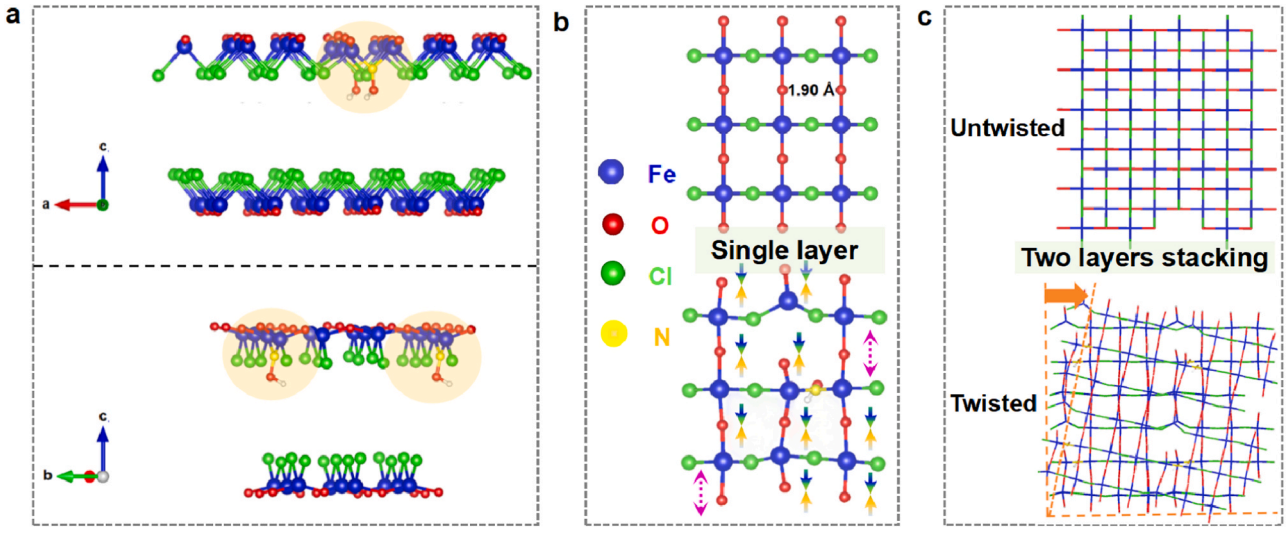

Fig. 3. The calculated crystal structure of FeOCl and HA-FeOCl. (a) The calculated lattice structures of HA-FeOCl viewed along [100] direction. (b) the bond length of Fe−O in FeOCl (up) and HA-FeOCl (down). (c) The stacking way of two 2D layers in FeOCl (up) and HA-FeOCl (down).

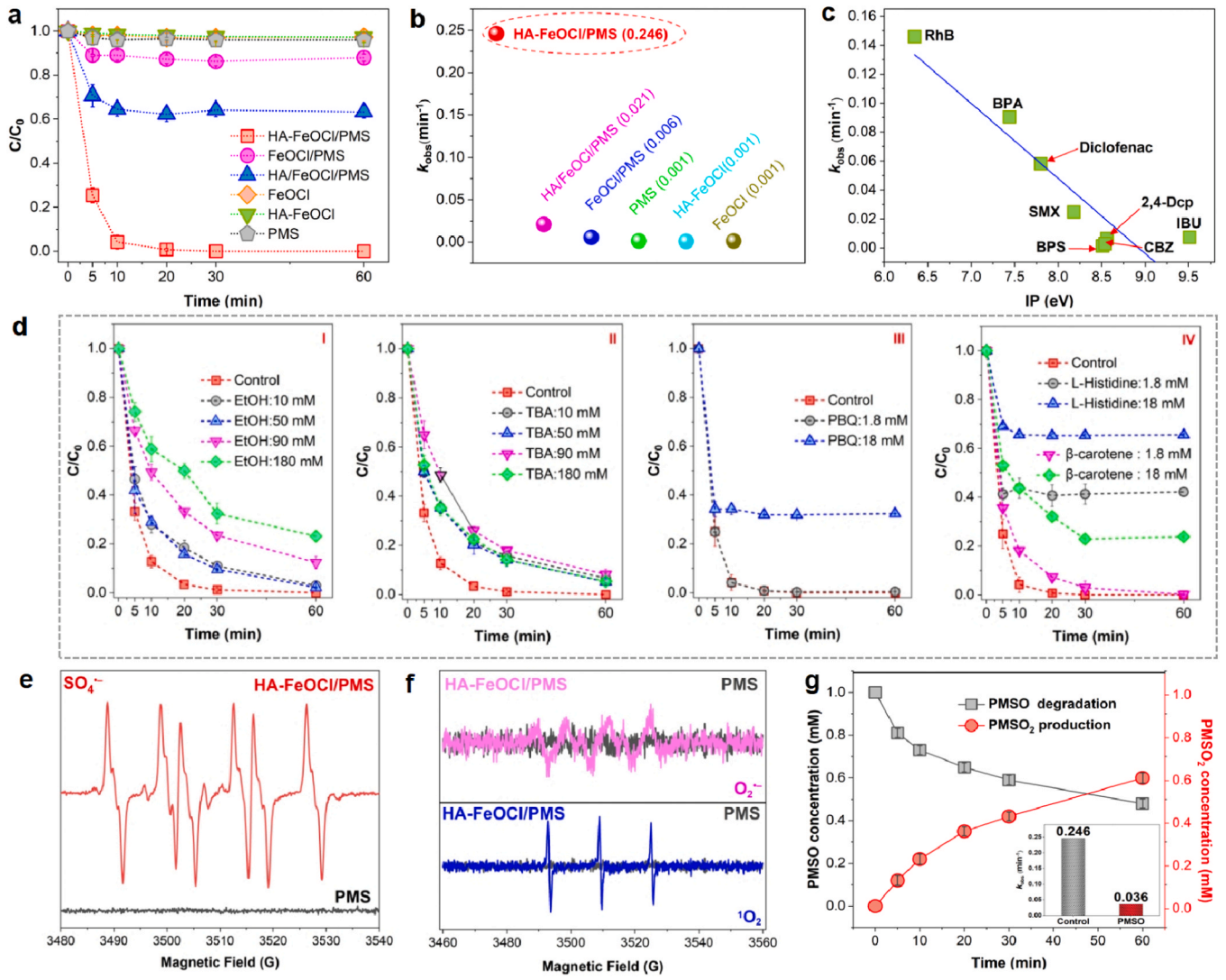

Fig. 4. Degradation catalytic performance. (a) Removal of BPA in different systems. (b) Comparison of the rate constants of BPA removal in different systems. (c) Relationship between the degradation rate of organics and their IP values. (d) Quenching tests in PMS activation for BPA degradation. e EPR spectra using DMPO for $SO_4^{\bullet-}$ and $^{\bullet}OH$. (f) EPR spectra using DMPO for $O_2^{\bullet-}$and TEMP for $^1O_2$. (g) PMSO degradation and corresponding $PMSO_2$ production.

~8.18 eV), which normally bear with higher electron donation ability. In a typical ROS involved system, pollutants tent to be degraded through pathways including electron-transfer, hydrogen abstraction and radical addition [4]. The preference to organics with lower IP values indicates that the involved ROS in the HA-FeOCl/PMS system tent to attack organics via electron transfer pathway. Besides, the zata potential of HA-FeOCl is 7.67 (Fig. S15), it means that the surface of the catalyst was always positively charged in the reaction solution. Consequently, for organics with higher pK_a values (i.e. BPS, CBZ), it would be harder to be degraded due to the lower affinity toward the catalyst surface.

To investigate the involved ROS in BPA degradation, Ethanol (EtOH), Tertiary butanol (TBA), and p-benzoquinone (p-BQ) were chosen as the quenching agents for $SO_4^{\bullet-}$, $^{\bullet}OH$, and $O_2^{\bullet-}$, respectively, while β-carotene and L-histidine were applied to quench $^1O_2$ (Fig. 4d). When 18 mM of β-carotene and L-histidine were introduced, the BPA removal dropped significantly to 79.7% and 57.8%, respectively. Similarly, after the introduction of EtOH (10 mM), TBA (10 mM) and p-BQ (1.8 mM), the BPA removal was inhibited to 97.1%, 93.4% and 99.5%, respectively, and with the increase of agent concentrations, the inhibition degree experienced obvious increase. These results imply that four ROS may have cooperated to degrade BPA in the HA-FeOCl/PMS system. The electron paramagnetic resonance (EPR) was adopted to inspect the radicals generation and evolution during BPA degradation. 5,5-Dimethyl-1-pyrroline-N-oxide (DMPO) was selected as the capture agent for $SO_4^{\bullet-}$, $^{\bullet}OH$, and $O_2^{\bullet-}$, and 2,2,6,6-tetramethyl-4-piperi-done (TEMP) was used for $^1O_2$. No radicals were detected when only PMS was present (Fig. 4e), while significant characteristic signals of DMPO-$SO_4^{\bullet-}$ showed up in the HA-FeOCl/PMS system, indicating that the efficient activation of PMS by HA-FeOCl rapidly generated $SO_4^{\bullet-}$. However, the typical signal peak of DMPO-$^{\bullet}OH$ with intensity of 1:2:2:1 was not observed. In addition, $^1O_2$ and $O_2^{\bullet-}$ signals were also detected (Fig. 4f). Apparently, the results of EPR test basically agree well with those of quenching tests.

Recent studies suggest that high valent Fe-oxo (Fe(IV)=O) may be involved in some homogeneously PMS activation systems by Fe^{2+} [36], which could be verified by a specific rapid reaction with PMSO to produce $PMSO_2$. In HA-FeOCl/PMS system (Fig. 4g), after 60 min of reaction, the PMSO concentration decreased significantly from 1 mM to 0.52 mM, and a large amount of $PMSO_2$ was also produced (from 0 mM to 0.62 mM). The results confirm the generation of Fe(VI) in the system. Meanwhile, since after the introduction of PMSO, the k_{obs} of BPA degradation decreased from 0.246 min^{-1} to 0.036 min^{-1} (inset), further demonstrating that Fe(IV) was involved in the BPA oxidation.

3.3. Mechanistic investigation

As is known, during the activation of PMS by Fe-based catalyst, the most critical first step is the electron-rich Fe sites donating electrons to the electron-deficient O—O bond in HSO_5^- and generating ROS (Eqs.2–3). Apparently, a ready chemical environment of Fe sites for electron donation can be crucial in deciding the ROS formation rate [25, 37,38]. Therefore, to elucidate the relationship between surface twisting and the promoted PMS catalytic activation, attention was paid onto the effect of distorted structure on charge transfer between HA-FeOCl and PMS.

$$Fe(II) + HSO_5^- \rightarrow Fe(III) + SO_4^{\bullet -} + OH^- \quad (2)$$

$$Fe(III) + HSO_5^- \rightarrow Fe(II) + SO_5^{\bullet -} + H^+ \quad (3)$$

According to the results of XAFS, Mössbauer spectra, and DFT calculation, due to the surface structural distortion, both of the geometrical configuration and the electronic orbit around Fe sites have became less symmetric, associating with an increased polarization onto the surface charge distribution [29]. It can be told from the changes in charge density distribution (Fig. 5a) from FeOCl to HA-FeOCl. The higher electron density around Fe in HA-FeOCl could be attributed to the mixing of 3d and 4p orbitals, which lead to the electron cloud distribution concentrating in some specific direction [39]. More importantly, the less symmetrical geometry can be more favorable for Fe to bonding due to the higher degree of freedom of valence electrons, which bears less constraint from the atom [40,41]. It normally dedicates a higher electron mobility of Fe sites [42–44] in HA-FeOCl, comparing to the more symmetrical ones in pristine FeOCl. When PMS molecular is absorbed onto the Fe sites, the charge transfer should therefore more intense.

To verify this, the PMS adsorption onto the surfaces of FeOCl and HA-FeOCl has been theoretically modeled (Fig. 5b), with the yellow and pink colors representing the electron depletion and electron accumulation, respectively. Clearly, the charge transfer between HA-FeOCl and PMS was stronger than that of FeOCl, which can be also reflected by the higher Bader charge of Fe in HA-FeOCl (1.8e vs 1.4e). On the other hand, in-situ electrochemical analyses (Fig. 5c, Figs. S11 and S16) were also conducted for verifying the boosted electron transfer experimentally. The open-circuit potentials of glassy carbon electrode (GCE) with FeOCl or HA-FeOCl catalysts coating immediately rose to 0.36 V and 0.40 V after adding PMS, and then decreased upon the addition of BPA. It confirms that the electron transfer between PMS and the coated GCE happened in both systems. While in contrast, the potential change in HA-FeOCl/PMS system (0.400 V) was obviously higher than those in FeOCl/PMS (0.352 V) and blank-GCE/PMS systems (0.325 V), demonstrating a stronger electron transfer as well as a greater interfacial reaction rate.

In a word, the formation of twisted surfaces onto FeOCl has changed its geometry structure from octahedral to the less symmetric tetrahedral (Fig. 5d), thus improving the freedom of electron around Fe atoms. It means that these active sites would be easier to donate electrons when associated with PMS, thus promoting the breakage of O—O bond.

DFT analysis was further carried out to unveil the catalytic pathways of ROS generation in two syestems. The optimized structure of the HA-FeOCl for the adsorption of HSO_5^-, as well as the structures of intermediates, transition states (TS) and products of ROS are shown in Fig. 5f (I) and Figs. S25 and S26. In both systems, the energy barriers (II and III) required to produce $SO_4^{\bullet -}$ were the lowest compared to the other ROS. After HSO_5^- was adsorbed on the catalysts surface, the bond length of $l_{O\text{-}O}$ both increased, but the energy barrier for $SO_4^{\bullet -}$ generation in HA-

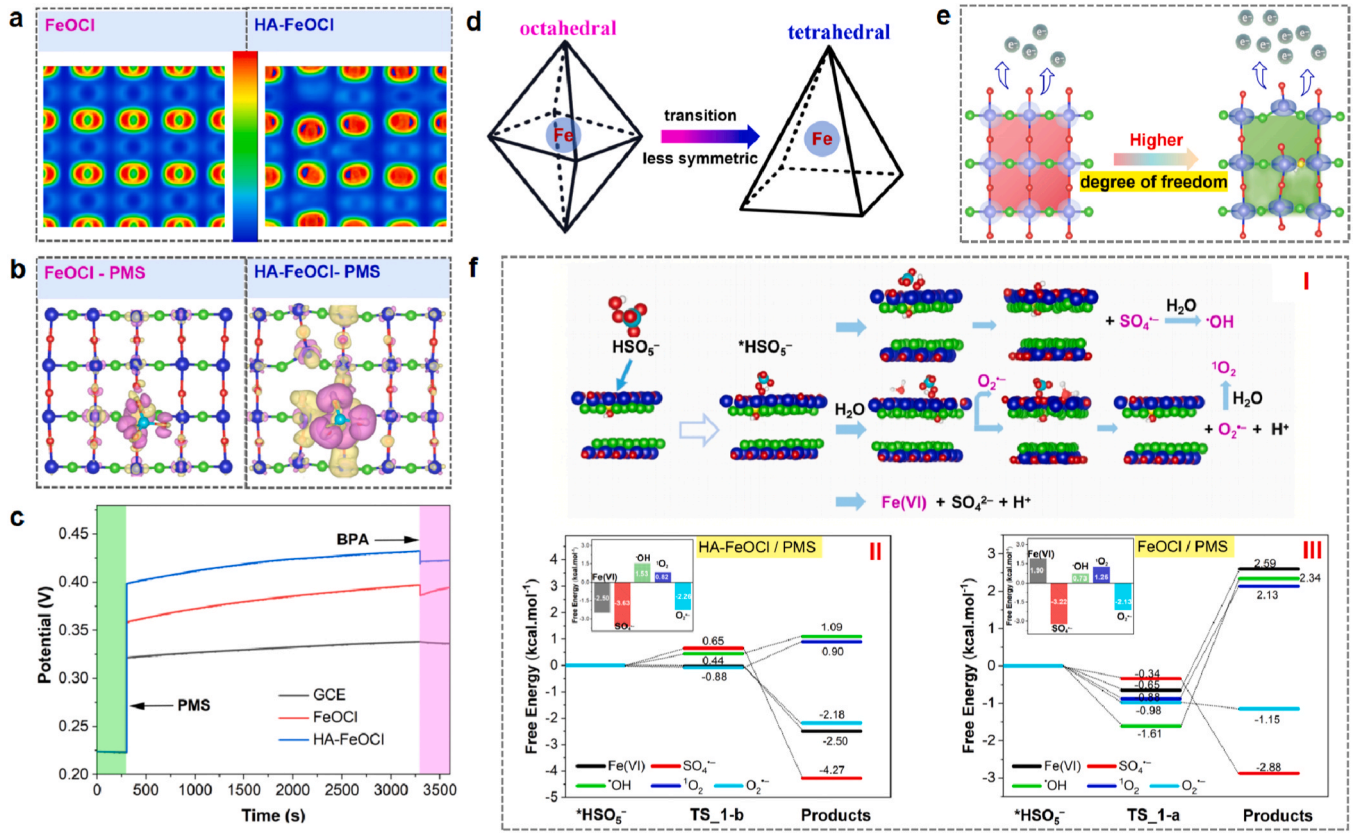

Fig. 5. Density functional theory calculation for the PMS activation mechanism. (a) Charge density maps at twisted surfaces of FeOCl (left) and HA-FeOCl (right) viewed along [100] direction. (b) Differential Charge density after PMS adsorption. (c) The change of open-circuit potential in different systems. (d) Variations in geometrical configuration of Fe. (e) The increased freedom of charge of electron. (f) The process of PMS activation by HA-FeOCl (I) and the energy profiles of ROS formation (II and III, inset: the total energy barrier of ROS).

FeOCl/PMS system was − 3.63 kcal/mol, being lower than that of FeOCl/PMS system at − 3.22 kcal/mol. It indicates that $SO_4^{\bullet-}$, as the primary ROS, is more readily produced in HA-FeOCl/PMS system. On the other hand, for both systems, the energy barrier values required for the formation of $^{\bullet}OH$ were the highest, which might be caused by the complexity of the generation of $^{\bullet}OH$. That is, $SO_4^{\bullet-}$ was firstly generated in the reaction and then reacted with H_2O to generate $^{\bullet}OH$ (Eq. 4).

$$SO_4^{\bullet-} + H_2O \rightarrow HSO_4^- + {}^{\bullet}OH \quad (4)$$

The generation of $*HSO_5^-$ is the essential first step in the generation of $O_2^{\bullet-}$ and $^1O_2$. According to Eqs.5–6, $*HSO_5^-$ could react with H_2O to produce HO_2^-, which further react with HSO_5^- to form $O_2^{\bullet-}$. In addition, the energy barrier value forming $^1O_2$ is higher than that of $O_2^{\bullet-}$, it might be due to the fact that $^1O_2$ is formed by the reaction of $O_2^{\bullet-}$ with H_2O (Eq. 7), which requires further absorption of energy in the reaction to complete the stable formation of $^1O_2$. Although the formation processes of $O_2^{\bullet-}$ and $^1O_2$ were similar to each other in both systems, their total energy barrier values were both lower in HA-FeOCl/PMS system (–2.26 kcal/mol< –2.13 kcal/mol for $O_2^{\bullet-}$ and 0.82 kcal/mol<1.25 kcal/mol for $^1O_2$). The differences in Fe(VI)=O production has also be revealed by the DFT results. When $*HSO_5^-$ was formed (Eq. 7), the reactant [$Fe^{(II)}$(HO_2SO_3)] undergo O−O bond and O−H bond dissociation to form Fe(VI)=O with energy barrier of 1.09 kcal/mol (HA-FeOCl/PMS) and 2.59 kcal/mol (FeOCl/PMS). And the total energy barrier for Fe(VI)=O formation were calculated to be –2.5 kcal/mol and 1.9 kcal/mol, respectively Therefore, though Fe (VI) has been tested in both systems, it is clearly more thermodynamically feasible to produce Fe (VI) in HA-FeOCl/PMS system.

$$Fe(III) + HSO_5^- + H_2O \rightarrow H^+ + Fe(II)\text{-}SO_3OH_2 + O_2^{\bullet-} \quad (5)$$

$$Fe(II)\text{-}SO_3OH_2 \rightarrow Fe(II) + SO_4^{2-} + 3\,H^+ + O_2^{\bullet-} \quad (6)$$

$$O_2^{\bullet-} + H_2O \rightarrow {}^1O_2 + 2OH^- + H_2O_2 \quad (7)$$

$$Fe(II) + HSO_5^- \rightarrow Fe(VI){=}O + SO_4^{2-} + H^+ \quad (8)$$

Apparently, HA-FeOCl with twisted surface has made most of the ROS generation from PMS activation more convenient, thus improving the reactivity of HA-FeOCl/PMS system toward organics oxidation.

4. Conclusions

In summary, we have demonstrated that the targeted fine-tuning of Fe sites on 2D layered FeOCl can be achieved through intercalation engineering, achieving effective PMS activation and efficient oxidation of OMCs with almost 41 orders of magnitude faster reaction kinetics than pristine FeOCl. The surfaces twisted have introduced the polarized charge distribution onto the base planes of FeOCl, which increases the degree of freedom of electron around Fe site, resulting in higher electron donation ability of FeOCl toward PMS for breaking the electron-deficient O—O bond. Accordingly, the energy barriers for primary ROS generation were lowered in the HA-FeOCl/PMS system, enabling much improved OMCs oxidation efficiencies. This work gives insight into the structure-property relationship of 2D ferrite with twisted surfaces, and highlights the concept of 2D-interface engineering for effective AOP catalyst design.

CRediT authorship contribution statement

Xu Ximeng: Writing – original draft, Methodology, Investigation, Formal analysis. **Zhang Shujing:** Methodology. **Zhang Wei:** Writing – review & editing, Resources. **Guan Qingqing:** Supervision, Methodology. **Wang Nana:** Methodology. **Wang Yuhao:** Formal analysis. **Liu Xiaohong:** Methodology. **Jiang Qinli:** Investigation, Formal analysis.

Declaration of Competing Interest

The authors declare that they have no known competing financial interests or personal relationships that could have appeared to influence the work reported in this paper.

Data availability

The data that support the findings of this study are available from the corresponding author upon reasonable request.

Acknowledgements

This work was supported by the National Natural Science Foundation of China (grant nos. 42177464 and 62175237), the Yunnan Fundamental Research Projects (grant no. 140520210219), the XinJiang Science Fund for Distinguished Young Scholars (grant no. 2022D01E40), the Key Research and Development Program of Yunnan Province (grant no. 202203AC100004), Natural Science Foundation of Chongqing, China (grant no. CSTB2023NSCQ-MSX0768), Natural Science Foundation of Chongqing China (grant no. cstc2021jcyj-jqX0031), Interdiscipline Team Project under auspices of "Light of West" Program in Chinese Academy of Sciences (grant no. xbzg-zdsys-202106), and Young Scholar of Regional Development Program in Chinese Academy of Sciences (grant no. 2021).

Appendix A. Supporting information

Supplementary data associated with this article can be found in the online version at doi:10.1016/j.apcatb.2024.123701.

References

[1] L. Yang, D. Xu, X. Luo, X. Zhu, J. Zhao, J. Song, Y. Han, G. Li, X. Gao, L. Liu, H. Liang, Fe(II)-modulated microporous electrocatalytic membranes for organic microcontaminant oxidation and fouling control: mechanisms of regulating electron transport toward enhanced reactive oxygen species activation, Environ. Sci. Technol. 57 (2023) 19000–19011.
[2] L. Zhu, Q. Yan, M. Ran, X. Liu, Y. Bao, X. Duan, M. Xing, Selective removal of ultrafine suspended solids during organic pollutant degradation by a MoS_2/graphene oxide sponge, Sci. Bull. 68 (2023) 892–896.
[3] J. Xu, Y. Yao, C. Zhu, L. Lu, Q. Fang, Z. He, S. Song, B. Chen, Y. Shen, Unveiling enhanced electron-mediated peroxymonosulfate activation for degradation of emerging organic pollutants, Appl. Catal. B Environ. 341 (2024) 123356.
[4] J. Lee, U. von Gunten, J.-H. Kim, Persulfate-based advanced oxidation: critical assessment of opportunities and roadblocks, Environ. Sci. Technol. 54 (2020) 3064–3081.
[5] N. Li, J. Ye, H. Dai, P. Shao, L. Liang, L. Kong, B. Yan, G. Chen, X. Duan, A critical review on correlating active sites, oxidative species and degradation routes with persulfate-based antibiotics oxidation, Water Res. 235 (2023) 119926.
[6] B. Shi, H. Li, X. Fu, C. Zhao, M. Li, M. Liu, W. Yan, H. Yang, Fe single-atom catalyst for cost-effective yet highly efficient heterogeneous Fenton catalysis, ACS Appl. Mater. Interfaces 14 (2022) 53767–53776.
[7] C. Chen, M. Yan, Y. Li, Y. Hu, J. Chen, S. Wang, X.L. Wu, X. Duan, Single-atom co sites confined in layered double hydroxide for selective generation of surface-bound radicals via peroxymonosulfate activation, Appl. Catal. B Environ. 340 (2024) 123218.
[8] X. Xie, J. Cao, Y. Xiang, R. Xie, Z. Suo, Z. Ao, X. Yang, H. Huang, Accelerated iron cycle inducing molecular oxygen activation for deep oxidation of aromatic VOCs in MoS_2 co-catalytic Fe^{3+}/PMS system, Appl. Catal. B Environ. 309 (2022) 121235.
[9] X. Long, Z. Xiong, R. Huang, Y. Yu, P. Zhou, H. Zhang, G. Yao, B. Lai, Sustainable Fe(III)/Fe(II) cycles triggered by co-catalyst of weak electrical current in Fe(III)/peroxymonosulfate system: Collaboration of radical and non-radical mechanisms, Appl. Catal. B Environ. 317 (2022) 121716.
[10] M. Huang, Y. Li, C. Zhang, C. Cui, Q. Huang, M. Li, Z. Qiang, T. Zhou, X. Wu, H. Yu, Facilely tuning the intrinsic catalytic sites of the spinel oxide for peroxymonosulfate activation: From fundamental investigation to pilot-scale demonstration, Proc. Natl. Acad. Sci. USA 119 (2022) e2202682119.
[11] X. Li, H. Rong, J. Zhang, D. Wang, Y. Li, Modulating the local coordination environment of single-atom catalysts for enhanced catalytic performance, Nano Res. 13 (2020) 1842–1855.
[12] L. Jiao, W. Xu, Y. Zhang, Y. Wu, W. Gu, X. Ge, B. Chen, C. Zhu, S. Guo, Boron-doped Fe-N-C single-atom nanozymes specifically boost peroxidase-like activity, Nano Today 35 (2020) 100971.

[13] J. Song, N. Hou, X. Liu, M. Antonietti, Y. Wang, Y. Mu, Unsaturated single-atom CoN_3 sites for improved fenton-like reaction towards high-valent metal species, Appl. Catal. B Environ. 325 (2023) 122368.
[14] S. Thambidurai, P. Gowthaman, M. Venkatachalam, S. Suresh, M. Kandasamy, Morphology dependent photovoltaic performance of zinc oxide-cobalt oxide nanoparticle/nanorod composites synthesized by simple chemical co-precipitation method, J. Alloy. Compd. 852 (2021) 156997.
[15] Q. Zhou, C. Song, P. Wang, Z. Zhao, Y. Li, S. Zhan, Generating dual-active species by triple-atom sites through peroxymonosulfate activation for treating micropollutants in complex water, Proc. Natl. Acad. Sci. USA 120 (2023) e2300085120.
[16] Y. Bao, C. Lian, K. Huang, H. Yu, W. Liu, J. Zhang, M. Xing, Generating high-valent Iron-oxo ≡FeIV=O complexes in neutral microenvironments through peroxymonosulfate activation by Zn−Fe layered double hydroxides, Angew. Chem. Int. Ed. 61 (2022) e202209542.
[17] Y. Yin, R. Lv, W. Zhang, J. Lu, Y. Ren, X. Li, L. Lv, M. Hua, B. Pan, Exploring mechanisms of different active species formation in heterogeneous Fenton systems by regulating iron chemical environment, Appl. Catal. B Environ. 295 (2021) 120282.
[18] Z. Zhao, J. Park, C. Choi, S. Hong, X. Hui, H. Zhang, T.W. Lo, A.W. Robertson, Z. Lv, Y. Jung, Z. Sun, Engineering vacancy and hydrophobicity of two-dimensional $TaTe_2$ for efficient and stable electrocatalytic N_2 reduction, Innovation 3 (2022) 2666–6758.
[19] X. Zou, Y. Xu, W. Duan, 2D materials: rising star for future applications, Innovation 2 (2021) 2666–6758.
[20] G. Lin, H. Li, K. Xie, Twisted surfaces in porous single crystals to deliver enhanced catalytic activity and stability, Angew. Chem. Int. Ed. 59 (2020) 16440–16444.
[21] F. Cheng, G. Lin, X. Hu, S. Xi, K. Xie, Porous single-crystalline titanium dioxide at 2 cm scale delivering enhanced photoelectrochemical performance, Nat. Commun. 10 (2019) 3618.
[22] M.S. Stark, K.L. Kuntz, S.J. Martens, S.C. Warren, Intercalation of layered materials from bulk to 2D, Adv. Mater. 31 (2019) 1808213.
[23] W. Yao, Y. Zhang, T. Lyu, W. Huang, N. Huang, X. Li, C. Zhang, F. Liu, M. Wuttig, Y. Yu, M. Hong, L. Hu, Two-step phase manipulation by tailoring chemical bonds results in high-performance GeSe thermoelectrics, Innovation 4 (2023) 2666–6758.
[24] J. Wang, K.-P. Hou, Y. Wen, H. Liu, H. Wang, K. Chakarawet, M. Gong, X. Yang, Interlayer structure manipulation of iron oxychloride by potassium cation intercalation to steer H_2O_2 activation pathway, J. Am. Chem. Soc. 144 (2022) 4294–4299.
[25] X. Xu, S. Zhang, Y. Wang, Y. Lin, Q. Guan, C. Chen, Identifying the role of surface hydroxyl on FeOCl in bridging electron transfer toward efficient persulfate activation, Environ. Sci. Technol. 57 (2023) 12922–12930.
[26] Y. Yin, Y. Ren, J. Lu, W. Zhang, C. Shan, M. Hua, L. Lv, B. Pan, The nature and catalytic reactivity of UiO-66 supported Fe_3O_4 nanoparticles provide new insights into Fe-Zr dual active centers in Fenton-like reactions, Appl. Catal. B Environ. 286 (2021) 119943.
[27] E.H. Frøen, P. Adler, M. Valldor, Synthesis and properties of $Ba_6Fe_2Te_3S_7$, with an Fe dimer in a magnetic singlet state, Inorg. Chem. 62 (2023) 12548–12556.
[28] Y. Zhang, J. Mao, E. Oldfield, 57Fe Mössbauer isomer shifts of heme protein model systems: electronic structure calculations, J. Am. Chem. Soc. 124 (2002) 7829–7839.
[29] A. Genoux, M. Pauly, C.L. Rooney, C. Choi, B. Shang, S. McGuigan, M.S. Fataftah, Y. Kayser, S.C.B. Suhr, S. DeBeer, H. Wang, P.A. Maggard, P.L. Holland, Well-defined iron sites in crystalline carbon nitride, J. Am. Chem. Soc. 145 (2023) 20739–20744.
[30] J.-H. Choy, J.-B. Yoon, D.-K. Kim, S.-H. Hwang, Application of X-ray absorption spectroscopy in determining the crystal structure of low-dimensional compounds. Iron oxychloride and its alkoxy substituents, Inorg. Chem. 34 (1995) 6524–6531.
[31] Y. Shiro, F. Sato, T. Suzuki, T. Iizuka, T. Matsushita, H. Oyanagi, X-ray absorption spectral study of ferric high-spin hemoproteins: XANES evidences for coordination structure of the heme iron, J. Am. Chem. Soc. 112 (1990) 2921–2924.
[32] J. Zhu, Z. Zeng, W.-X. Li, K-edge XANES investigation of fe-based oxides by density functional theory calculations, J. Phys. Chem. C 125 (2021) 26229–26239.
[33] J. Roh, A. Cho, S. Kim, K.-S. Lee, J. Shin, J.S. Choi, J. Bak, S. Lee, D. Song, E.-J. Kim, C. Lee, Y.R. Uhm, Y.-H. Cho, J.W. Han, E. Cho, Transformation of the active Moiety in phosphorus-doped Fe–N–C for highly efficient oxygen reduction reaction, ACS Catal. 13 (2023) 9427–9441.
[34] J. Wang, M. Tsai, Z. Lu, Y. Li, G. Huang, H. Wang, H. Liu, X. Liao, B. Hwang, A. Neumann, X. Yang, pH-dependent structure–activity relationship of polyaniline-intercalated FeOCl for heterogeneous Fenton reactions, ACS Omega 4 (2019) 21945–21953.
[35] Z. Tang, P. Zhao, H. Wang, Y. Liu, W. Bu, Biomedicine meets Fenton chemistry, Chem. Rev. 121 (2021) 1981–2019.
[36] K. Qian, H. Chen, W. Li, Z. Ao, Y. Wu, X. Guan, Single-atom Fe catalyst outperforms its homogeneous counterpart for activating peroxymonosulfate to achieve effective degradation of organic contaminants, Environ. Sci. Technol. 55 (2021) 7034–7043.
[37] F. Deng, H. Olvera-Vargas, M. Zhou, S. Qiu, I. Sirés, E. Brillas, Critical review on the mechanisms of Fe2+ regeneration in the electro-Fenton process: fundamentals and boosting strategies, Chem. Rev. 123 (2023) 4635–4662.
[38] K. Hou, Z. Pi, F. Chen, L. He, F. Yao, S. Chen, X. Li, H. Dong, Q. Yang, Sulfide enhances the Fe(II)/Fe(III) cycle in Fe(III)-peroxymonosulfate system for rapid removal of organic contaminants: treatment efficiency, kinetics and mechanism, J. Hazard. Mater. 435 (2022) 128970.
[39] H. Gu, G. Shi, L. Zhong, L. Liu, H. Zhang, C. Yang, K. Yu, C. Zhu, J. Li, S. Zhang, C. Chen, Y. Han, S. Li, L. Zhang, A two-dimensional van der Waals heterostructure with isolated electron-deficient cobalt sites toward high-efficiency CO_2 electroreduction, J. Am. Chem. Soc. 144 (2022) 21502–21511.
[40] Z. Guo, Y. Si, W. Xia, F. Wang, H. Liu, C. Yang, W. Zhang, W. Li, Electron delocalization triggers nonradical Fenton-like catalysis over spinel oxides, Proc. Natl. Acad. Sci. USA 119 (2022) e2201607119.
[41] D.A. Kuznetsov, B. Han, Y. Yu, R.R. Rao, J. Hwang, Y. Román-Leshkov, Y. Shao-Horn, Tuning redox transitions via inductive effect in metal oxides and complexes, and implications in oxygen electrocatalysis, Joule 2 (2018) 225–244.
[42] W. Qu, W. Liu, H. Wen, X. Qu, Y. Guo, Z. Tang, L. Hu, S. Tian, C. He, D. Shu, Boosting Fenton-like Catalysis Via Electron Tunneling-based C–Co charge-transfer bridge in nitrogen-doped cobalt@carbon nanotube-grafted carbon polyhedron, ACS EST Eng. 3 (2023) 213–225.
[43] L. Wu, Z. Sun, Y. Zhen, S. Zhu, C. Yang, J. Lu, Y. Tian, D. Zhong, J. Ma, Oxygen vacancy-induced nonradical degradation of organics: critical trigger of oxygen (O_2) in the Fe–Co LDH/peroxymonosulfate system, Environ. Sci. Technol. 55 (2021) 15400–15411.
[44] Z. Chen, W. Zhang, C. Wei, Y. Zhou, Y. Pan, X. Wei, J. Huang, L. Wang, G. Yu, High-electron mobility tetrafluoroethylene-containing semiconducting polymers, Chem. Mater. 32 (2020) 2330–2340.